RSC Advances

PAPER

View Article Online
View Journal | View Issue

Check for updates

Cite this: *RSC Adv.*, 2017, 7, 49675

CNTs based improved chlorine sensor from non-covalently anchored multi-walled carbon nanotubes with hexa-decafluorinated cobalt phthalocyanines

Anshul Kumar Sharma,[a] Aman Mahajan,*[a] R. K. Bedi,[a] Subodh Kumar,[b] A. K. Debnath[c] and D. K. Aswal[d]

Received 14th August 2017
Accepted 10th October 2017

DOI: 10.1039/c7ra08987b

rsc.li/rsc-advances

To study the effect of synergetic interactions between metal-phthalocyanine and carbon nanotubes for gas sensing characteristics of carbon nanotubes, we synthesized a hybrid of cobalt(II)-1,2,3,4,8,9,10,11,15,16,17,18,22,23,24,25-hexa-decafluoro-29*H*,31*H*-phthalocyanine/multi-walled carbon nanotubes ($F_{16}CoPc$/MWCNTs–COOH). The as-prepared hybrid was characterized through spectroscopic (FT-IR, UV-vis and Raman), electron microscopic (TEM and FE-SEM) and TGA investigations that confirmed the successful non-covalent anchoring of $F_{16}CoPc$ onto MWCNTs–COOH through π–π stacking interactions. Further, a highly reversible, reproducible, sensitive and Cl_2 selective chemiresistive sensor was fabricated using $F_{16}CoPc$/MWCNTs–COOH hybrid, which exhibited a sensitivity of ~63% for 2 ppm of Cl_2 and a limit of detection as low as 0.05 ppb. A plausible gas sensing mechanism for improved gas sensing characteristics of $F_{16}CoPc$/MWCNTs–COOH sensor towards Cl_2 was explained using Raman, X-ray photoelectron spectroscopy (XPS) and electrochemical impedance spectroscopy (EIS) studies. Herein, cobalt metal ion is found to play an important role in enhancing gas sensing characteristics of the fabricated sensor.

1. Introduction

Concern for environmental pollution, medical diagnosis, automobiles and industrial emission monitoring has led to the development of sensors that can detect chemical species in the atmosphere.[1,2] Thus, it is of great concern for the development of sensors that are rapid, simple and consume low power. In this direction, nanostructured CNTs based chemiresistive sensors stand out due to their unique and interesting properties, such as large specific surface area, gas adsorption capability and high electrical conductivity.[3] Chemiresistive sensors are comparatively rapid, cheap and simple to use having low power consumption and temperature requirements[4] in comparison to analytical procedure based on high-performance liquid chromatography-mass spectrometry (HPLC-MS) or gas chromatography-mass spectrometry (GC-MS), both of which are quite laborious, expensive and cumbersome.[5] A number of gases such as NO_2, NH_3, NO, CO and Cl_2 have been tested using CNTs based chemiresistive sensors.[6–9] However, poor sensing characteristics (lack of selectivity, irreversibility and slow response/recovery time) due to low charge transfer between the pristine CNTs and gas molecules hamper commercialization of CNTs based sensors. Further, a variety of methods have been developed for making CNT networks, such as direct growth on substrates, dispersions, electrophoresis and Langmuir–Blodgett.[5] However, limitations to these methods are the requirement of expensive and specific equipment for mounting CNTs directly on substrates. The primary hurdles in solution-based methods are poor solubility of CNTs in solvents and very less stability of dispersions of CNTs. To improve the solubility and gas sensing characteristics of CNTs based sensors, hybrids of CNTs with materials, such as metal oxides, noble metal nanoparticles and organic semiconductors, have been explored.[10–13]

The CNTs based hybrid gas sensors have attracted extensive attention due to synergic effects of two or more components through the strong electron transfer interaction.[14]

Hsu *et al.*[15] have monitored the residual chlorine concentration using phenyl-capped aniline tetramer (PCAT) doped with SWCNTs in drinking water with detection range of 0.06–60 mg l^{-1}. Muñoz *et al.*[16] demonstrated the capability of modified MWCNTs nanocomposite sensors with CuO nanoparticles for the sensitive sensing of free chlorine. Li *et al.*[17] have reported the Cl_2 selective hybrid of single-wall carbon nanotubes (SWCNTs) with polymers such as chlorosulfonated

---

[a] Material Science Laboratory, Department of Physics, Guru Nanak Dev University, Amritsar, 143005, India. E-mail: aman.phy@gndu.ac.in
[b] Department of Chemistry, Guru Nanak Dev University, Amritsar, 143005, India
[c] Technical Physics Division, Bhabha Atomic Research Centre, Mumbai, 400085, India
[d] CSIR-National Physical Laboratory, New Delhi, 115012, India

polyethylene and hydroxypropyl cellulose as chemiresistive sensors but were having primary issues of response and recovery time with these sensors. Furthermore, Gohier *et al.*[18] have reported MWCNTs as well as nitrogen-doped and polyethyleneimine (PEI) functionalized MWCNTs based room temperature Cl_2 sensor that can detect a Cl_2 concentration down to 27 ppb, but sensor recovery could only be possible by heating it up to 75 °C for 60 min. In spite of various efforts, the characteristics such as gas response, selectivity and stability are still not ideal.

These challenging issues of improving carbon nanotube sensing characteristics have initiated to explore hybrids of carbon nanotubes with metallo-phthalocyanines (MPcs). MPcs are extensively used as excellent sensing materials as they exhibit remarkable gas sensing characteristics due to their fascinating chemical and physical properties and good thermal and chemical stability.[19] Moreover, solubility of hybrids is better in comparison with pristine CNTs, which make them more attractive for different applications.[20] The simple solution processing methods such as solution assembly, dip dropping and spin coating can be used for deposition of hybrid films. Recently, we have fabricated ppb level chemiresistive Cl_2 sensor using substituted phthalocyanine and CNTs based hybrids.[21–24] Further, the central metal ion, substitution of functional groups on phthalocyanine ring, influences the morphology and remarkably tunes the gas sensing characteristics of phthalocyanine molecules.[25]

In the present study, multi-walled carbon nanotubes (MWCNTs–COOH) are non-covalently functionalized with Co(II)-1,2,3,4,8,9,10,11,15,16,17,18,24,25-hexa-decafluoro-29*H*,31*H*-phthalocyanine (F_{16}CoPc) for fabrication of ppb level Cl_2 selective chemiresistive sensor. In comparison to our earlier reports, F_{16}CoPc molecule proved to be a better material for CNTs functionalization because of tuneable electronic properties due to shorter π–π stacking inter-molecular distance (~3.23 Å).[26,27] Moreover, molecular functionalization causes molecular orbitals to get closer to the Fermi level that leads to an increase in its ionization potential and electron affinity.[28]

2. Experimental

The commercially available MWCNTs and F_{16}CoPc samples were procured from Sigma-Aldrich Pvt. Ltd., India. Furthermore, acidification of MWCNTs bearing an acidic group (–COOH) was carried out according to the multi-step procedures developed by Smalley and co-workers.[29] F_{16}CoPc/MWCNTs–COOH hybrid was synthesized using solution assembly method through π–π stacking between MWCNTs–COOH and F_{16}CoPc in DMF. Herein, varied amount of F_{16}CoPc (0.1 to 0.5 wt%) was dissolved in 5 ml of dimethylformamide (DMF) and subjected to ultra-sonication, to form F_{16}CoPc solution in DMF. This solution was then added dropwise to MWCNTs–COOH suspensions in DMF and the resulting mixtures were sonicated at room temperature (25 °C) for 3 h and subsequently stirred in dark for 6 h at 80 °C. The mixture was filtered through a PTEF filter (0.22 μm, Millipore) and washed thoroughly with DMF to remove excess of F_{16}CoPc derivative, subsequently rinsed with ethanol for several times and finally dried to acquire desired, F_{16}CoPc/MWCNTs–COOH hybrid.

Fourier transform infrared (FT-IR) spectra were acquired on Perkin Elmer Frontier FT-IR spectrometer. Raman spectroscopic measurements were carried out using Renishaw invia micro-Raman spectrometer. Ultraviolet-visible (UV-vis) spectra were recorded on the UV-1601PC (Shimadzu, Japan) spectrophotometer. The morphology of F_{16}CoPc/MWCNTs–COOH hybrid is obtained by field-emission scanning electron microscopy (FE-SEM, Carl Zeiss, supra 55) and transmission electron microscopy (TEM, Jeol, TEM-2100). Thermo gravimetric analysis (TGA) was carried out using a thermogravimetry analyzer (Hitachi STA 7200) under a nitrogen atmosphere from 40 to 900 °C at a scan rate of 10 °C min^{-1}. X-ray photoelectron spectroscopy (XPS) was performed using Mg K_α X-ray beams as the excitation source (1253.6 eV) and MAC2 electron analyzer system attached to MBE machine (EVA-32 Riber, France). The binding energy scale was calibrated to Au $4f_{7/2}$ line of 84.0 eV.

The gas sensing studies were performed in a home-built stainless steel test chamber (1000 ml) containing sample holder geometry as shown in Fig. 1. To fabricate the gas sensor, 2 mg of the as-prepared F_{16}CoPc/MWCNTs–COOH hybrid was dispersed in 1 ml of DMF and then 30 μL of the above solution was poured onto the glass substrate with two pre-coated gold electrodes (3 mm × 3 mm at a spacing of 1 mm) and then allowed to dry at ambient temperature. The silver wires were connected to the gold electrodes using silver paste. The effective area of the sensor was 3 mm × 1 mm. Sensor resistance was recorded continuously by applying a constant bias of 3 V during both dosing and purging cycles as a function of time using computer interfaced Keithley electrometer 6517A. The internal temperature of test chamber is monitored by a thermocouple. A desired concentration of (Cl_2, NO_2, NO, C_2H_5OH, H_2S, CO and NH_3) gases in the test chamber was achieved by injecting a known quantity of gas using a micro-syringe. After exposure, once a steady state was achieved, sensor resistance was recovered by opening the lid of the test chamber. The response of the gas sensor was calculated using the eqn (1);

$$S\,(\%) = |(R_a - R_g)/R_a| \times 100 \tag{1}$$

here, R_a and R_g represent the sensor resistance in air and gas environment, respectively. The response time is the time required for sensor resistance to reach 90% of its equilibrium

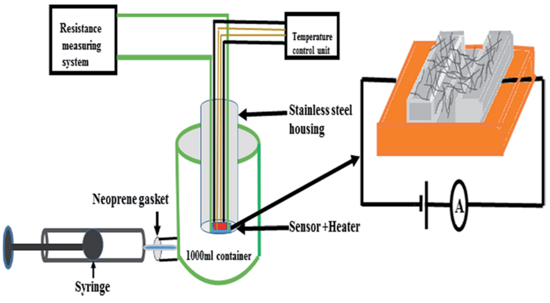

Fig. 1 Gas sensing set-up used in the present study.

value after the gas is introduced into the test chamber and the recovery time was measured as the time required for the sensor resistance to regain 90% of its original value after the removal of gas. XPS study of exposed samples was performed by *ex situ* exposure of gases to the samples in gas sensing set-up (Fig. 1) and transferring them to XPS analysis chamber. Electrochemical impedance spectroscopy study was performed using a frequency response analyzer (FRA) attached with a potentiostat (Autolab) in the frequency range of 10 Hz to 1 MHz.

3. Results and discussion

3.1 Characterization of $F_{16}CoPc$/MWCNTs–COOH hybrid

Fig. 2 shows the FTIR spectra of $F_{16}CoPc$, MWCNTs–COOH and $F_{16}CoPc$/MWCNTs–COOH hybrid. The observed IR peaks for $F_{16}CoPc$ (Fig. 2(a)) at positions 498, 605, 754, 845, 965 and 1158 cm^{-1} correspond to hexa-decafluoro substituents and two strong bands at 1496 and 1325 cm^{-1} correspond to the stretching of C=C and C=N, respectively; the other observed characteristic peaks at 1283, 1529 and 1622 cm^{-1} are attributed to phthalocyanine macrocycles.[14,30,31] The MWCNTs–COOH (Fig. 2(b)) shows a peak at 1037 cm^{-1} corresponding to C–O stretching vibration, a peak at 3440 cm^{-1} due to the O–H stretching; the characteristic peak at 1637 cm^{-1} due to C=C stretching confirmed the graphitic structure of CNTs.[32] The presence of peaks at 2855 and 2921 cm^{-1} are attributed to the asymmetric and symmetric CH_2 stretching in CNTs.[32,33] The peaks appearing in $F_{16}CoPc$ and MWCNTs–COOH (Fig. 2(c)) can be found in $F_{16}CoPc$/MWCNTs–COOH hybrid and are observed to be red shifted in the wave-numbers in comparison to their individual peaks due to electron delocalization by π–π interaction between $F_{16}CoPc$ and CNTs. This observation demonstrates that $F_{16}CoPc$ molecules were successfully anchored onto the surface of MWCNTs–COOH.[34]

To study the interaction between $F_{16}CoPc$ molecules and MWCNTs–COOH, Raman spectra of $F_{16}CoPc$/MWCNTs–COOH hybrid was compared with those of $F_{16}CoPc$ and MWCNTs–COOH (Fig. 3). The peaks at 143, 176, 208, 283, 470, 513, 587, 680, 738 and 965 cm^{-1} in $F_{16}CoPc$ sample were obtained due to vibrations of isoindole moieties.[35] The peaks between 1200 and 1600 cm^{-1} correspond to pyrrole groups and a band at 1544 cm^{-1} corresponds to cobalt ion, which is in good agreement with reported studies.[36,37] Raman spectra of MWCNTs–COOH exhibit the characteristic G-band (related to C–C vibration of the carbon material with a sp^2 orbital structure) around 1593 cm^{-1} and D band (associated with sp^2 C with defects) around 1360 cm^{-1}.[38,39] Comparison of Raman spectra of the hybrid with $F_{16}CoPc$ and MWCNTs–COOH shows a combination of their individual characteristic Raman peaks with a change in peak positions and their intensities. The intensity ratio of D band to the G band (I_D/I_G), known as a ratio of sp^3-hybridized carbon atom relative to sp^2-bonded carbon atom, is found to be 1.16 and 1.31 for MWCNTs–COOH and hybrid sample, respectively.[40,41] This small variation of I_D/I_G ratio indicated that $F_{16}CoPc$ were attached to the surface of MWCNTs–COOH through a non-covalent modification.[40]

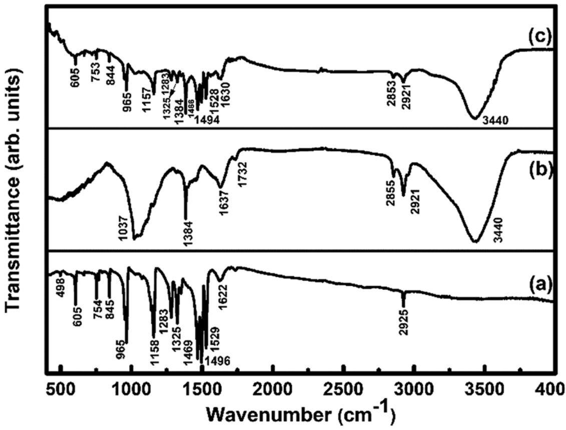

Fig. 2 FTIR spectra of (a) $F_{16}CoPc$; (b) MWCNTs–COOH and (c) $F_{16}CoPc$/MWCNTs–COOH hybrid.

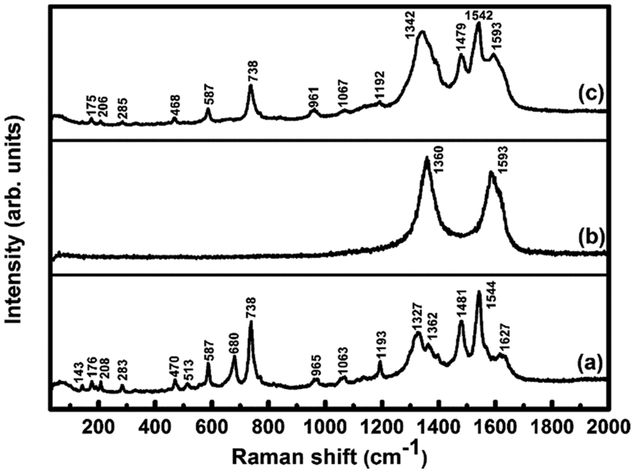

Fig. 3 Raman spectra of (a) $F_{16}CoPc$; (b) MWCNTs–COOH and (c) $F_{16}CoPc$/MWCNTs–COOH hybrid.

Fig. 4 depicts the UV-visible absorption spectra of $F_{16}CoPc$, MWCNTs–COOH and $F_{16}CoPc$/MWCNTs–COOH hybrid. The

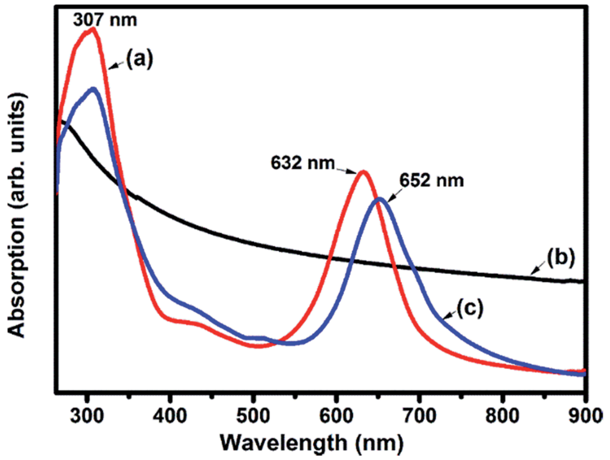

Fig. 4 UV-visible absorption spectra of (a) $F_{16}CoPc$; (b) MWCNTs–COOH and (c) $F_{16}CoPc$/MWCNTs–COOH hybrid.

UV-visible spectrum of F_{16}CoPc exhibited two strong absorption bands; one broad B band in the wavelength at around 307 nm due to the electronic transitions from the highest occupied molecular orbital (HOMO) a_{2u} to the lowest unoccupied molecular orbital (LUMO) e_g level and the other Q band doublet at around 632 nm arising from the electronic transitions from HOMO a_{1u} level to LUMO e_g level.[42] The UV-visible absorption spectra of MWCNTs–COOH has been found to be featureless.[43] However, in case of hybrids, the Q-band is found to be comparatively broadened and red shifted by 20 nm as compared to that of F_{16}CoPc. This observation is concomitant with an expanded macrocyclic conjugated structure of F_{16}CoPc and reduced energy difference between the HOMO and the LUMO to facilitate charge transfer between the F_{16}CoPc macrocycle and CNTs due to the π–π interaction.[30,40]

Fig. 5(a) shows TEM image of MWCNTs–COOH which are primarily empty long tubes with a mean diameter of 14 nm. The morphological features of the investigated hybrid (Fig. 5(b)) highlight the exo-hedral coverage of F_{16}CoPc molecules on the sidewalls of MWCNTs–COOH with a mean diameter of about 40 nm in comparison to MWCNTs–COOH, confirming the anchoring of 26 nm thick F_{16}CoPc molecules on MWCNTs–COOH. Further, Fig. 5(c) shows the SEM image of MWCNTs–COOH arranged in the groups of long tubular-shaped structures. The SEM image of F_{16}CoPc/MWCNT–COOH hybrid (Fig. 5(d)) reveals that F_{16}CoPc molecules are anchored on the surface of MWCNTs–COOH matrix making MWCNTs–COOH surface thicker and are in consonance with the TEM investigations.

The weight loss as a function of temperature for F_{16}CoPc, MWCNTs–COOH and F_{16}CoPc/MWCNTs–COOH hybrid materials was investigated using TGA plots (Fig. 6). An overall weight loss of 49.05% up to 900 °C is observed for F_{16}CoPc (Fig. 6(a)) comprising major weight losses between 200 to 330 °C and 366 to 604 °C, corresponding to desorption of adsorbed water and the decomposition of F_{16}CoPc, respectively.[20,44,45] TGA plots of MWCNTs–COOH (Fig. 6(b)) exhibit a weight loss of about 8.11% due to destruction of the residual carbon and decarboxylation of oxidized species,[45] whereas F_{16}CoPc/MWCNTs–COOH (Fig. 6(c)) shows a weight loss of 23.93% on heating the hybrid to 900 °C, corresponding to decomposition of the F_{16}CoPc on MWCNTs–COOH surface.[20]

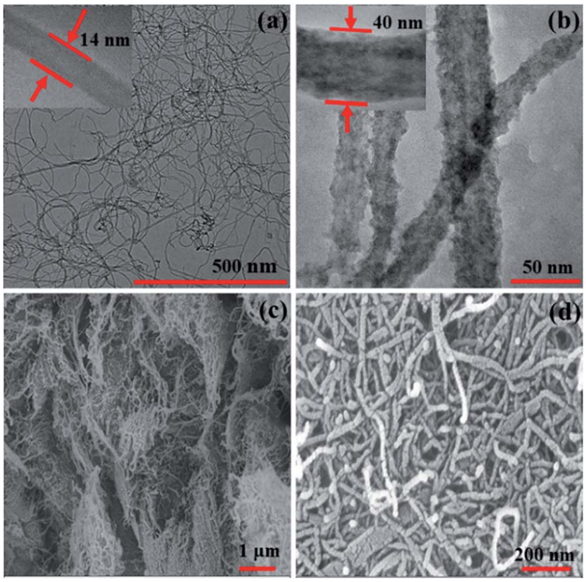

Fig. 5 TEM images of (a) MWCNTs–COOH and (b) F_{16}CoPc/MWCNTs–COOH hybrid (inset shows magnified view), and SEM images of (c) MWCNTs–COOH and (d) F_{16}CoPc/MWCNTs–COOH hybrid.

Further, the amount of F_{16}CoPc molecule absorbed on the MWCNTs–COOH was calculated using the ratio of difference in weight loss between MWCNTs–COOH and F_{16}CoPc/MWCNTs–COOH hybrid to weight loss for F_{16}CoPc and was found to be 32.23%.

3.2 Gas sensing properties of F_{16}CoPc/MWCNTs–COOH hybrid

To discuss the gas sensing characteristics of fabricated sensors (F_{16}CoPc/MWCNTs–COOH), we exposed them to 500 ppb of different test gases (Cl_2, NO_2, NO, H_2S, C_2H_5OH, NH_3 and CO) at room temperature (25 °C). The selectivity histogram for the observed responses of the sensor for these test gases is shown in Fig. 7(a). It can be noted from the histogram that 0.3 wt% F_{16}CoPc/MWCNTs–COOH sensor exhibits the best response among all the prepared sensors towards Cl_2, with a sensitivity value of ∼26% and was subsequently chosen for further sensing characterization. For all other test gases, the sensitivity value was <4%. Nevertheless, the sensor exhibited an irreversible behaviour at room temperature as it was not able to recover to its baseline resistance value even after a long interval of time. Moreover, recovery characteristics of the sensor were found to be greatly improved on heating. In such a situation, to make the sensor reversible, the operating temperature of the sensors was optimized. To find an optimum operating temperature, we exposed the sensor to 500 ppb of Cl_2 at different operating temperatures ranging from 30 to 200 °C and maximum

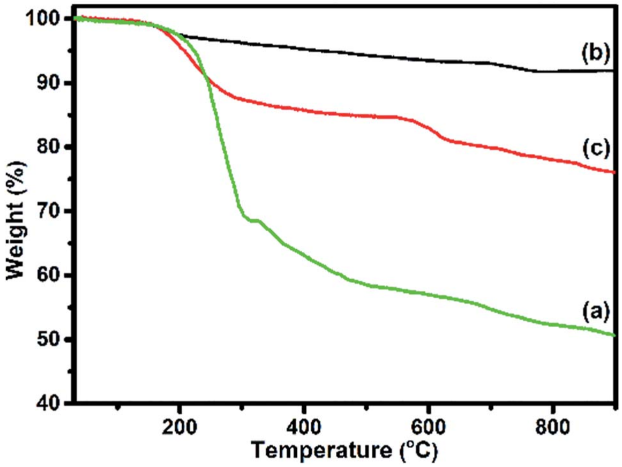

Fig. 6 TGA curves of (a) F_{16}CoPC; (b) MWCNTs–COOH and (c) F_{16}CoPc/MWCNTs–COOH hybrid.

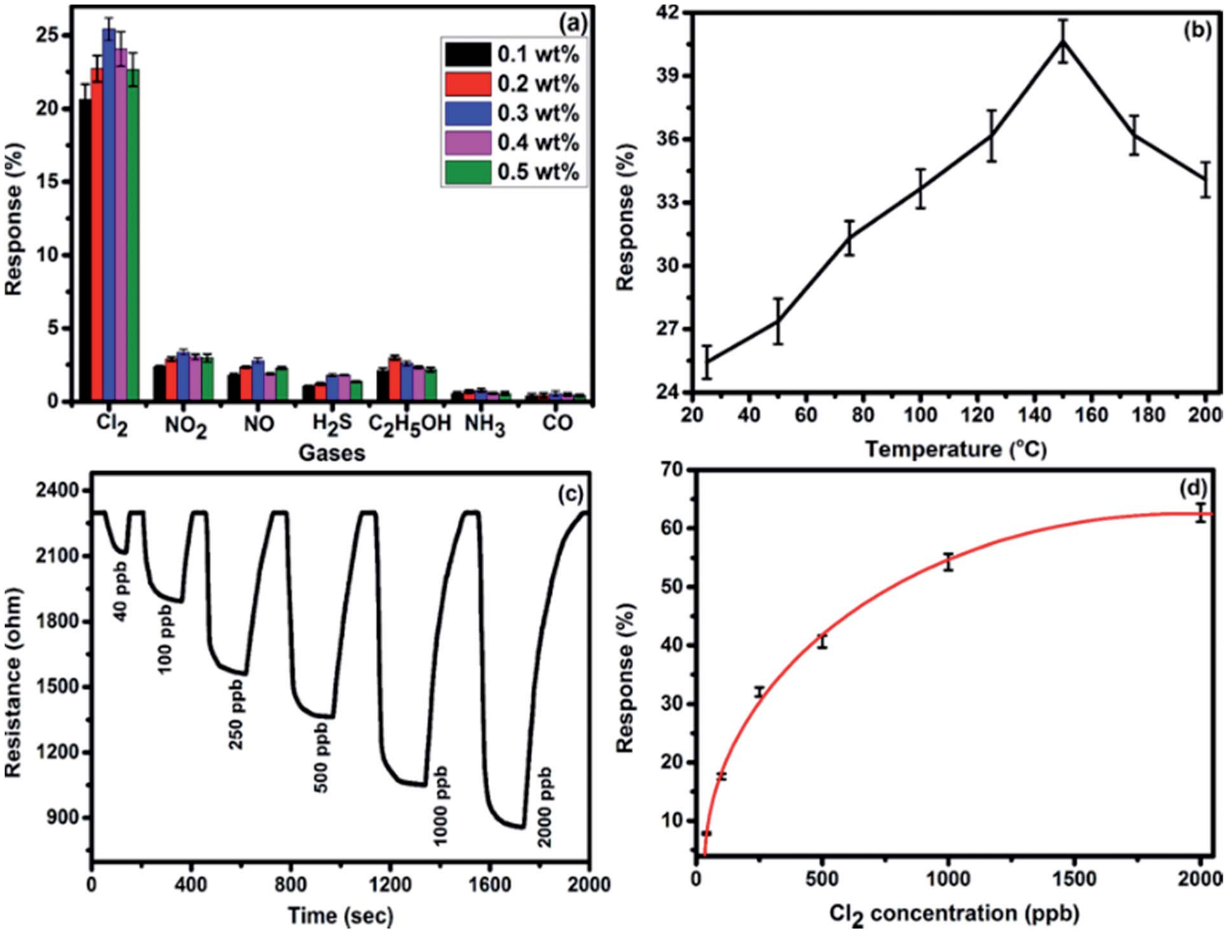

Fig. 7 (a) Selectivity histogram of F_{16}CoPc/MWCNTs–COOH sensors for 500 ppb of Cl_2, NO_2, NO, C_2H_5OH, H_2S, NH_3 and CO at room temperature. (b) Sensor response as a function of temperature for 500 ppb of Cl_2 concentration. (c) Response curves of sensor for different doses of Cl_2 at 150 °C. (d) Variation in the response of sensor with Cl_2 concentration (experimental curve (dotted lines) and fitting curve (solid lines)). (The standard error bars indicate the response variations using three times repeated testing of three sensor devices).

response of ~41% was obtained at a temperature of 150 °C (Fig. 7(b)). Furthermore, sensor response was observed to decrease beyond 150 °C due to desorption of Cl_2 from sensor surface. Fig. 7(c) shows the variation of response curve for different doses of Cl_2 (40–2000 ppb) at 150 °C. It demonstrates that there is a decrease in the sensor resistance after exposure to Cl_2 and it gets saturated after some time and again starts approaching to its initial baseline value after removal of Cl_2, which reveals the good reversibility of sensor.

Fig. 7(d) exhibits the response behaviour of F_{16}CoPc/MWCNTs–COOH sensor to 40–2000 ppb concentrations of Cl_2 at 150 °C, which indicates its increased response with the increase in Cl_2 concentration. This behaviour can be explained on the basis of surface area and the number of effective occupancy of active sites available on the sensor film provided by phthalocyanine molecules anchored on MWCNTs–COOH, which is in good agreement with the morphological study of the hybrid.[46]

There is lesser coverage of surface area at a lower concentration of Cl_2 and hence it interacts with lesser number of active sites available on sensor surface, leading to lower response. Nevertheless, at a higher concentration, Cl_2 covers comparatively larger surface area and interacts with larger number of active sites leading to higher sensor response.

Fig. 8 shows the response curves of F_{16}CoPc/MWCNTs–COOH sensor for successive exposures of Cl_2 in order to investigate the reproducibility of the sensor. The nearly same value of sensor response without any drift in the baseline resistance indicates the reproducible response characteristics of the sensor.

Furthermore, response variation with the gas concentration was studied using eqn (2)[47,48]

$$\frac{\Delta R}{R} = \alpha[\mathrm{Cl_2}]^{\beta} \tag{2}$$

where α and β are coefficients that depend on operating temperature and testing material. The constant α is adsorption capacity and β is the strength of adsorption,[48] and they were calculated by curve fitting of response curve. The smaller the value of β, the greater is the expected heterogeneity; the value of β lies between 0 and 1 for normal adsorption. The values of α and β are found to be 1.25 and 0.53, respectively. The value of

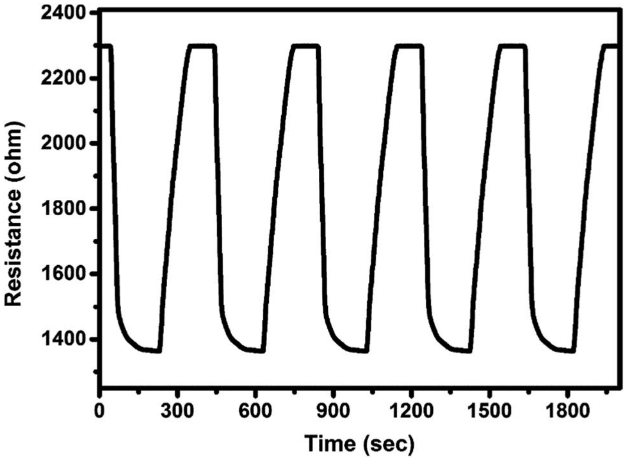

Fig. 8 Reproducibility of the response curve of F_{16}CoPc/MWCNTs–COOH sensor to 500 ppb of Cl_2 at 150 °C.

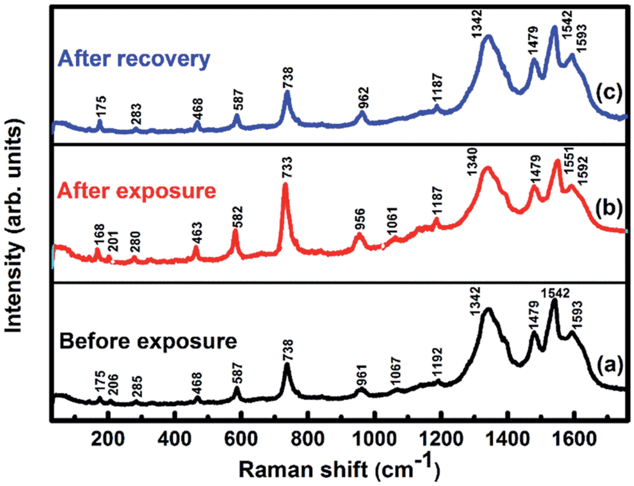

Fig. 9 Raman spectra of F_{16}CoPc/MWCNTs–COOH sensor recorded (a) before exposure; (b) after exposure to 25 ppm of Cl_2 and (c) after full recovery.

β is lesser than one, which indicates the normal mode of adsorption on the heterogeneous surface of sensor.[47]

The lowest detectable concentration of the sensor is dependent on the experimental set up used. Further, the limit of detection (LOD) of the sensor has been derived from signal-to-noise ratio (S/N). The signal-to-noise ratio is defined as $\Delta R/\sigma$, where ΔR is the maximum resistance change with respect to R_0 (baseline resistance) and σ refers to the root mean square (rms) noise of the baseline before exposure to gas.[49]

LOD is calculated using eqn (3);[50]

$$\text{LOD} = \frac{3 \times \text{concentration}}{\frac{\text{S}}{\text{N}}} \tag{3}$$

The signal-to-noise ratio of the sensor was 2400 and the theoretical detection limit of sensor was calculated to be 0.05 ppb.

3.3 Gas sensing mechanism

The underlying gas sensing mechanism of the sensor was investigated using XPS, Raman and impedance spectroscopy carried out before and after exposure to Cl_2. The comparison of Raman spectra (Fig. 9) of the unexposed sample with the exposed sample shows a shift in position of some peaks after Cl_2 exposure. On Cl_2 exposure, the peak corresponding to cobalt–nitrogen bond[51] at 175 cm^{-1} is found to shift by 7 cm^{-1} and peaks of macro-cyclic vibrations[52] (206, 285, 468, 587, 738, 961 and 1192 cm^{-1}) are shifted by 5 cm^{-1}, whereas D and G band corresponding to MWCNTs–COOH at 1342 and 1593 cm^{-1} are shifted by 2 and 1 cm^{-1}, respectively.[38,39] The significant shift of 9 cm^{-1} is observed for the Raman peak at 1542 cm^{-1}, which is due to displacement of C–N–C bridge bond, closely linked to the central metal ion of phthalocyanine molecule.[53] This observation is concomitant with the predominant interaction of Cl_2 with the cobalt ions of the hybrid sensor. Raman spectrum of the hybrid, recorded after removing Cl_2, exhibits identical peaks as detected in fresh samples, which indicates the good reversibility of the sensor.

Furthermore, X-ray photoelectron spectroscopy (XPS) (Fig. 10) of fresh F_{16}CoPc/MWCNTs–COOH hybrid possesses peaks at 284.8, 532.4, 399.2, 687.0, 780.7 and 795.9 eV corresponding to C-1s, O-1s, N-1s, F-1s, Co-$2p_{3/2}$ and Co-$2p_{1/2}$ levels, respectively.[54,55] In addition, on Cl_2 exposure, there is a peak shift of 0.2 eV in the spectrum of core level C-1s, a shift of 0.1 eV in spectrum of O-1s and F-1s, a shift of 0.3 eV in spectrum of N-1s and a prominent peak shift of 0.8 eV in the core level spectrum of Co-2p. The major shift of 0.8 eV towards higher BE side in the Co-2p core level and shifting of peak position of nitrogen, oxygen and fluorine spectrum towards higher binding energy confirms that charge transfer interaction occurs upon adsorption of strong electron acceptor Cl_2 molecules[55] onto the hybrid, leading to decrease in electron density due to transfer of electrons from hybrid to Cl_2. Thus, the study of Raman and XPS spectroscopic investigations demonstrate that on adsorption of Cl_2, charge transfer takes place between Cl_2 and hybrid through central metal cobalt ion.[55] Herein, the charge can favourably travel from CNTs to F_{16}CoPc, leading to an increase in hole concentration in CNTs and this results in fast variation of sensor resistance (Fig. 7(c)).[55,56] Moreover, it has been observed that XPS spectrum, recorded after recovery shows no shifting of peak position and absence of any chlorine signal confirms that the sensing process is highly reproducible.

As demonstrated, in morphological studies, the sensing layer consists of grains of F_{16}CoPc/MWCNTs–COOH and their respective grain boundaries. Nevertheless, exact contribution of these grains and grain boundaries towards sensing mechanism can be calculated by impedance spectroscopy of the prepared sensor. Fig. 11 shows Cole–Cole plot[46,57] between imaginary components of impedance ($-Z''$) as a function of real component (Z') of F_{16}CoPc/MWCNTs–COOH sensor in the presence of air and after exposure to 500 ppb of Cl_2. These plots exhibit a single semi-circle before and after exposure to Cl_2; their equivalent circuit consisting of RC network in series with a resistor R_0 is shown in the inset in Fig. 11. Herein, R_0 is the

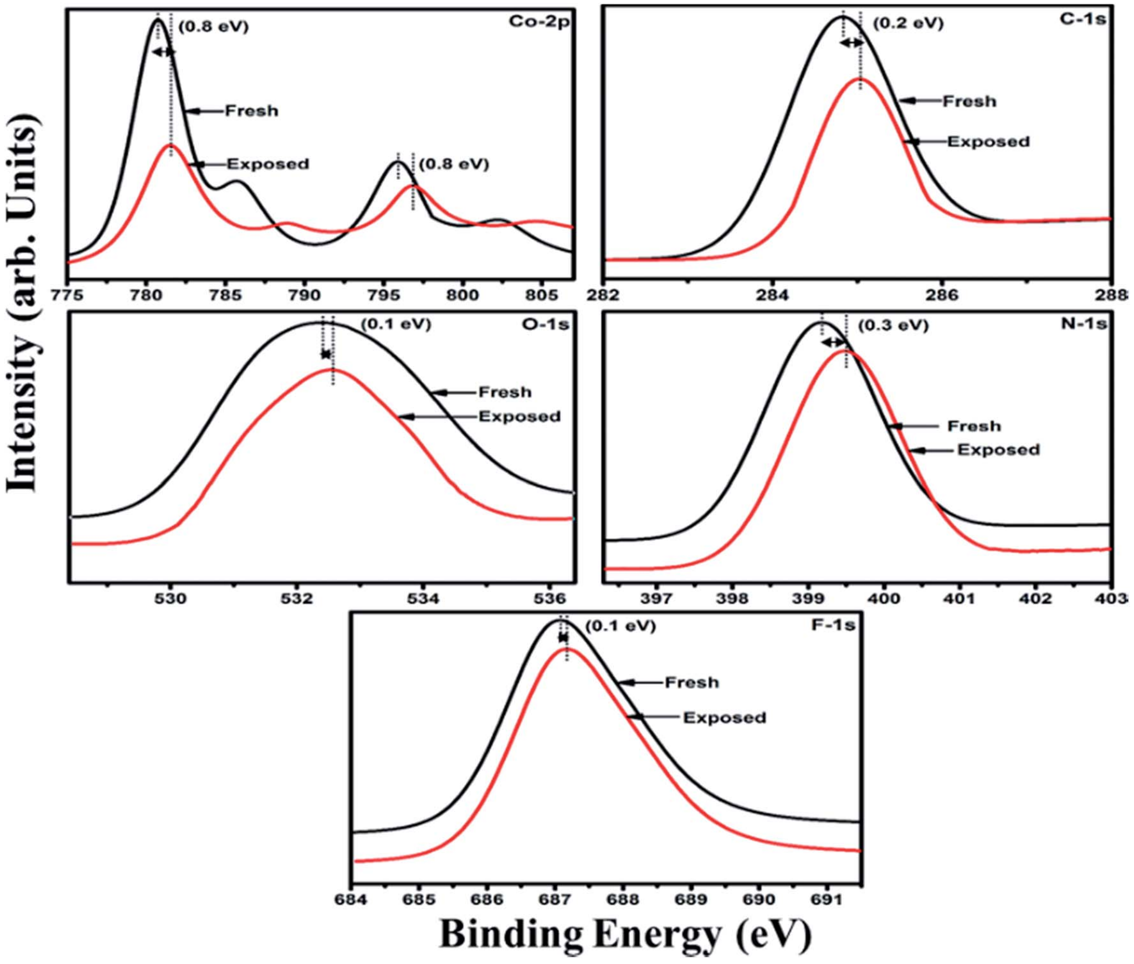

Fig. 10 XPS spectra of $F_{16}CoPc/MWCNTs-COOH$ sensor recorded before and after exposure to 25 ppm of Cl_2.

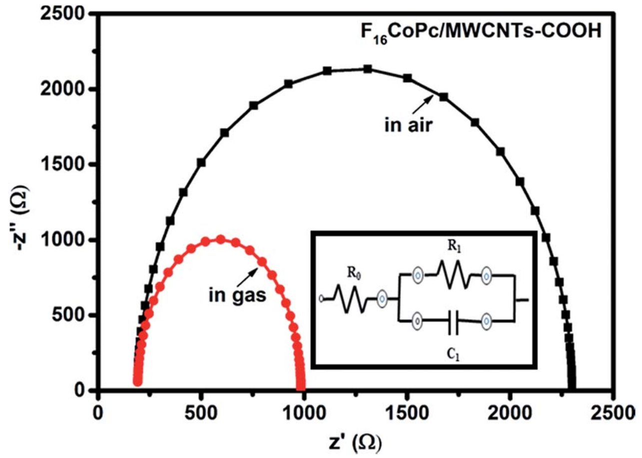

Fig. 11 Impedance spectra of fresh and Cl_2 exposed $F_{16}CoPc/MWCNTs-COOH$ sensor (inset shows the equivalent circuit used for analysis of data obtained from $F_{16}CoPc/MWCNTs-COOH$ sensor).

grain resistance and can be estimated from the intercept of the semi-circle at high frequency with the real axis. R_1 and C_1 are resistance and capacitance across grain boundaries, where R_1 can be determined from the diameter of the arc in Fig. 11, while C_1 can be calculated from the relation $\omega_{\max}R_1C_1 = 1$, where $\omega_{\max}$ is the frequency corresponding to the top of the arc.[57] The obtained values of R_0, R_1 and C_1 for the sensor using equivalent circuit are tabulated in Table 1.

The mathematical formulation for this equivalent circuit[46] can be given as follows:

$$Z = Z' + jZ'' \tag{4}$$

where,

$$Z' = R_0 + [R_1/(1 + \omega R_1C_1)^2]$$

and

$$Z'' = [\omega R_1^{\,2}C_1/(1 + \omega R_1C_1)^2]$$

It has been observed that the parameter R_0 remained nearly the same in air and in the presence of Cl_2, whereas R_1 decreases and C_1 increases on exposure to Cl_2 gas. This can be addressed on the basis of incoming Cl_2 adsorbed onto the grains outer surfaces leading to transfer of electron from hybrid to Cl_2 and

Table 1 Impedance parameters obtained for $F_{16}CoPc$/MWCNTs–COOH sensor by fitting experimental data to the equivalent circuit

		Parameters		
Sensor	Conditions	R_0 (Ω)	R_1 (Ω)	C_1 (nF)
$F_{16}CoPc$/MWCNTs–COOH	Unexposed	192	2108	3.34
	Exposed to 500 ppb Cl_2	192	792	7.15

improves the hole-conductivity through charge transfer between phthalocyanines and MWCNTs–COOH in concomitant with XPS results.[57]

Comparatively, a drastic fall in resistance (R_1) across grain boundary along with larger shift in BE (0.8 eV) and Raman shift (9 cm^{-1}) of cobalt ion on exposing the $F_{16}CoPc$/MWCNTs–COOH[23] sensor to Cl_2 in comparison to $F_{16}CuPc$/MWCNTs–COOH–[23] and $F_{16}ZnPc$/MWCNTs–COOH–[24] based sensor establish the formation of an efficient charge transfer between $F_{16}CoPc$/MWCNTs–COOH sensor and Cl_2 to make an improved chlorine sensor.

4. Conclusions

In conclusion, we have explored $F_{16}CoPc$ as functional moieties for the non-covalent functionalization of CNTs through the solution assembly method and subsequently the $F_{16}CoPc$/MWCNTs–COOH hybrid was investigated as ppb-level Cl_2 sensor. In comparison to $F_{16}CuPc$/MWCNTs–COOH and $F_{16}ZnPc$/MWCNTs–COOH sensors, the present results demonstrate that the $F_{16}CoPc$/MWCNTs–COOH sensor exhibits high sensitivity (62.66% for 2 ppm with LOD of 0.05 ppb), excellent reproducibility and selectivity. X-ray photoelectron, Raman and electrochemical impedance spectroscopic studies revealed the efficient charge transfer between $F_{16}CoPc$/MWCNTs–COOH sensor and chlorine. These outcomes underline the potential of such hybrid material in developing a new low cost Cl_2 sensor with excellent gas sensing characteristics.

Conflicts of interest

There are no conflict to declare.

Acknowledgements

The authors are thankful to Council of Scientific and Industrial Research (CSIR), New Delhi, India for providing financial assistance to accomplish this research work.

Notes and references

1 Z. Ting, M. Syed, V. M. Nosang and A. D. Marc, *Nanotechnology*, 2008, **19**, 332001.
2 A. Kumar, A. Singh, A. K. Debnath, S. Samanta, D. K. Aswal, S. K. Gupta and J. V. Yakhmi, *Talanta*, 2010, **82**, 1485–1489.
3 S. Iijima, *Nature*, 1991, **354**, 56–58.
4 A. Das, R. Dost, T. H. Richardson, M. Grell, D. C. Wedge, D. B. Kell, J. J. Morrison and M. L. Turner, *Sens. Actuators, B*, 2009, **137**, 586–591.
5 J. G. Weis, J. B. Ravnsbæk, K. A. Mirica and T. M. Swager, *ACS Sens.*, 2016, **1**, 115–119.
6 A. L. Ndiaye, C. Varenne, P. Bonnet, É. Petit, L. Spinelle, J. Brunet, A. Pauly and B. Lauron, *Thin Solid Films*, 2012, **520**, 4465–4469.
7 E. S. Snow, F. K. Perkins, E. J. Houser, S. C. Badescu and T. L. Reinecke, *Science*, 2005, **307**, 1942–1945.
8 N. H. Quang, M. Van Trinh, B.-H. Lee and J.-S. Huh, *Sens. Actuators, B*, 2006, **113**, 341–346.
9 Z. J. Han, H. Mehdipour, X. Li, J. Shen, L. Randeniya, H. Y. Yang and K. Ostrikov, *ACS Nano*, 2012, **6**, 5809–5819.
10 R. Leghrib, A. Felten, J. J. Pireaux and E. Llobet, *Thin Solid Films*, 2011, **520**, 966–970.
11 M. Penza, G. Cassano, R. Rossi, M. Alvisi, A. Rizzo, M. A. Signore, T. Dikonimos, E. Serra and R. Giorgi, *Appl. Phys. Lett.*, 2007, **90**, 173123.
12 B. Wang, Y. Wu, X. Wang, Z. Chen and C. He, *Sens. Actuators, B*, 2014, **190**, 157–164.
13 A. K. Sharma, R. Saini, R. Singh, A. Mahajan, R. K. Bedi and D. K. Aswal, *AIP Conf. Proc.*, 2014, **1591**, 671–673.
14 X. Liang, Z. Chen, H. Wu, L. Guo, C. He, B. Wang and Y. Wu, *Carbon*, 2014, **80**, 268–278.
15 L. H. H. Hsu, E. Hoque, P. Kruse and P. Ravi Selvaganapathy, *Appl. Phys. Lett.*, 2015, **106**, 063102.
16 J. Muñoz, F. Céspedes and M. Baeza, *Microchem. J.*, 2015, **122**, 189–196.
17 J. Li, Y. Lu and M. Meyyappan, *IEEE Sens. J.*, 2006, **6**, 1047–1051.
18 A. Gohier, J. Chancolon, P. Chenevier, D. Porterat, M. Mayne-L'Hermite and C. Reynaud, *Nanotechnology*, 2011, **22**, 105501.
19 A. Yazc, N. Unus, A. Altndal, B. Salih and O. Bekaroglu, *Dalton Trans.*, 2012, **41**, 3773–3779.
20 E. N. Kaya, T. Basova, M. Polyakov, M. Durmus, B. Kadem and A. Hassan, *RSC Adv.*, 2015, **5**, 91855–91862.
21 R. Saini, A. Mahajan, R. K. Bedi, D. K. Aswal and A. K. Debnath, *Sens. Actuators, B*, 2014, **198**, 164–172.
22 R. Saini, A. Mahajan, R. K. Bedi, D. K. Aswal and A. K. Debnath, *RSC Adv.*, 2014, **4**, 15945–15951.
23 A. K. Sharma, A. Mahajan, R. Saini, R. K. Bedi, S. Kumar, A. K. Debnath and D. K. Aswal, *Sens. Actuators, B*, 2018, **255**, 87–99.
24 A. K. Sharma, A. Mahajan, R. K. Bedi, S. Kumar, A. K. Debnath and D. K. Aswal, *Appl. Surf. Sci.*, 2018, **427**, 202–209.
25 B. Kadem, M. Göksel, A. Şenocak, E. Demirbaş, D. Atilla, M. Durmuş, T. Basova, K. Shanmugasundaram and A. Hassan, *Polyhedron*, 2016, **110**, 37–45.
26 H. Jiang, J. Ye, P. Hu, F. Wei, K. Du, N. Wang, T. Ba, S. Feng and C. Kloc, *Sci. Rep.*, 2014, **4**, 7573.
27 P. A. Pandey, L. A. Rochford, D. S. Keeble, J. P. Rourke, T. S. Jones, R. Beanland and N. R. Wilson, *Chem. Mater.*, 2012, **24**, 1365–1370.

28 D. G. de Oteyza, A. El-Sayed, J. M. Garcia-Lastra, E. Goiri, T. N. Krauss, A. Turak, E. Barrena, H. Dosch, J. Zegenhagen, A. Rubio, Y. Wakayama and J. E. Ortega, *J. Chem. Phys.*, 2010, **133**, 214703.

29 J. Liu, A. G. Rinzler, H. Dai, J. H. Hafner, R. K. Bradley, P. J. Boul, A. Lu, T. Iverson, K. Shelimov, C. B. Huffman, F. Rodriguez-Macias, Y.-S. Shon, T. R. Lee, D. T. Colbert and R. E. Smalley, *Science*, 1998, **280**, 1253–1256.

30 Z. Yang, H. Pu, J. Yuan, D. Wan and Y. Liu, *Chem. Phys. Lett.*, 2008, **465**, 73–77.

31 Y. Wan, Q. Liang, Z. Li, S. Xu, X. Hu, Q. Liu and D. Lu, *J. Mol. Catal. A: Chem.*, 2015, **402**, 29–36.

32 Z. Zhao, Z. Yang, Y. Hu, J. Li and X. Fan, *Appl. Surf. Sci.*, 2013, **276**, 476–481.

33 M. Penza, R. Rossi, M. Alvisi, M. A. Signore, G. Cassano, D. Dimaio, R. Pentassuglia, E. Piscopiello, E. Serra and M. Falconieri, *Thin Solid Films*, 2009, **517**, 6211–6216.

34 P. Li, Y. Ding, A. Wang, L. Zhou, S. Wei, Y. Zhou, Y. Tang, Y. Chen, C. Cai and T. Lu, *ACS Appl. Mater. Interfaces*, 2013, **5**, 2255–2260.

35 M. Anghelone, D. Jembrih-Simbürger and M. Schreiner, *Spectrochim. Acta, Part A*, 2015, **149**, 419–425.

36 S. Tuncel, E. N. Kaya, M. Durmus, T. Basova, A. G. Gurek, V. Ahsen, H. Banimuslem and A. Hassan, *Dalton Trans.*, 2014, **43**, 4689–4699.

37 M. Szybowicz and J. Makowiecki, *J. Mater. Sci.*, 2012, **47**, 1522–1530.

38 A. Wang, Y. Wang, W. Yu, Z. Huang, Y. Fang, L. Long, Y. Song, M. P. Cifuentes, M. G. Humphrey, L. Zhang, J. Shao and C. Zhang, *RSC Adv.*, 2016, **6**, 20120–20127.

39 P. C. Eklund, J. M. Holden and R. A. Jishi, *Carbon*, 1995, **33**, 959–972.

40 Y. Wang, N. Hu, Z. Zhou, D. Xu, Z. Wang, Z. Yang, H. Wei, E. S.-W. Kong and Y. Zhang, *J. Mater. Chem.*, 2011, **21**, 3779–3787.

41 V. Datsyuk, M. Kalyva, K. Papagelis, J. Parthenios, D. Tasis, A. Siokou, I. Kallitsis and C. Galiotis, *Carbon*, 2008, **46**, 833–840.

42 H. Banimuslem, A. Hassan, T. Basova, A. D. Gülmez, S. Tuncel, M. Durmuş, A. G. Gürek and V. Ahsen, *Sens. Actuators, B*, 2014, **190**, 990–998.

43 T. Mugadza and T. Nyokong, *Electrochim. Acta*, 2009, **54**, 6347–6353.

44 B.-P. Jiang, L.-F. Hu, D.-J. Wang, S.-C. Ji, X.-C. Shen and H. Liang, *J. Mater. Chem. B*, 2014, **2**, 7141–7148.

45 J.-Q. Zeng, S.-N. Sun, J.-P. Zhong, X.-F. Li, R.-X. Wang, L.-N. Wu, L. Wang and Y.-J. Fan, *Int. J. Hydrogen Energy*, 2014, **39**, 15928–15936.

46 A. T. Mane, S. T. Navale, S. Sen, D. K. Aswal, S. K. Gupta and V. B. Patil, *Org. Electron.*, 2015, **16**, 195–204.

47 D. Kumar, P. Chaturvedi, P. Saho, P. Jha, A. Chouksey, M. Lal, J. S. B. S. Rawat, R. P. Tandon and P. K. Chaudhury, *Sens. Actuators, B*, 2017, **240**, 1134–1140.

48 I. Sayago, H. Santos, M. C. Horrillo, M. Aleixandre, M. J. Fernández, E. Terrado, I. Tacchini, R. Aroz, W. K. Maser, A. M. Benito, M. T. Martínez, J. Gutiérrez and E. Muñoz, *Talanta*, 2008, **77**, 758–764.

49 F. Rigoni, S. Tognolini, P. Borghetti, G. Drera, S. Pagliara, A. Goldoni and L. Sangaletti, *Analyst*, 2013, **138**, 7392–7399.

50 G. Chen, T. M. Paronyan, E. M. Pigos and A. R. Harutyunyan, *Sci. Rep.*, 2012, **2**, 343.

51 G. S. S. Saini, S. Sukhwinder, K. Sarvpreet, K. Ranjan, S. Vasant and S. K. Tripathi, *J. Phys.: Condens. Matter*, 2009, **21**, 225006.

52 R. Kötz and E. Yeager, *J. Electroanal. Chem. Interfacial Electrochem.*, 1980, **113**, 113–125.

53 M. Szybowicz, W. Bała, K. Fabisiak, K. Paprocki and M. Drozdowski, *J. Mater. Sci.*, 2011, **46**, 6589–6595.

54 J.-H. Yang, Y. Gao, W. Zhang, P. Tang, J. Tan, A.-H. Lu and D. Ma, *J. Phys. Chem.*, 2013, **117**, 3785–3788.

55 R. A. Hatton, N. P. Blanchard, V. Stolojan, A. J. Miller and S. R. P. Silva, *Langmuir*, 2007, **23**, 6424–6430.

56 A. L. Verma, S. Saxena, G. S. S. Saini, V. Gaur and V. K. Jain, *Thin Solid Films*, 2011, **519**, 8144–8148.

57 N. H. Al-Hardan, M. J. Abdullah and A. A. Aziz, *Int. J. Hydrogen Energy*, 2010, **35**, 4428–4434.